Lab on a Chip

PAPER

View Article Online
View Journal | View Issue

Cite this: *Lab Chip*, 2026, **26**, 1996

Bone-on-leaf-chip for the study of lung cancer bone metastasis

Qi Liu,[ab] Di Suo,[ab] Renxian Wang,[c] Shuai Zhao,[ab] Mao Mao,[d] Wei-Ning Lee,[c] Yuhe Yang*[ab] and Xin Zhao *[abe]

Organ-on-a-chip systems provide invaluable preclinical insights into disease simulation, mechanism investigation and drug screening. By closely simulating the physiological conditions of human organs, these platforms enhance our understanding of complex biological processes. Here, we applied a leaf vein microfluidic chip as a controllable, endothelialized *in vitro* platform to investigate how hierarchical flow distribution and uniform shear influence tumor cell migration and behavior within a bone-mimetic microenvironment as a model demonstration. The hierarchical leaf vein architecture, resembling mammalian blood vessels, enables mechanistic studies of spatial distribution and migration under physiologically relevant conditions. Additionally, the system incorporates specialized chambers embedded with 3D hydrogel containing human umbilical vein endothelial cells (HUVECs) and bone stromal cells (HS-5) as the dormancy niche, and HUVECs and osteoclast precursor cells (THP-1) as the "vicious cycle" niche. These chambers serve as a demonstration of bone-mimetic units for examining specific microenvironmental responses. These bone microenvironments were modified by conditioned medium (CM) from primary tumor cells, facilitating their roles as the bone pre-metastatic niche. Cell morphology of lung cancer cells (A549) was observed throughout the dynamic culture process. Perfused medium and hydrogels were harvested to investigate the potential mechanisms. For the dormancy niche, the upregulation of angiogenin, MIP-3α, Wnt-5a, and TGF-β2 and the downregulation of CCL7 indicated that tumor-secreted factors may reactivate dormant tumor cells by activating angiogenesis, pro-inflammatory, and epithelial–mesenchymal transition related pathways. These changes in OPN and BMP-1 expression suggested potential involvement in bone microenvironment remodeling which were inferred from cytokine and gene expression profiles. For the "vicious cycle" niche, the upregulation of CCL5, CXCL5 and VCAM-1 may be associated with the recruitment of leukocytes and promotion of tumor invasion, based on cytokine profiling. These cytokines can serve as potential biomarkers for assessing disease progression or providing a basis for developing new targeted therapies. Taken together, the successful construction and application of this leaf vein chip establish a versatile, mechanistically tractable platform for future drug screening, pathological analysis, and microenvironment-targeted strategies relevant to bone metastasis.

Received 8th October 2025,
Accepted 8th February 2026

DOI: 10.1039/d5lc00951k

rsc.li/loc

Introduction

Cancer is one of the leading health problems, which caused 16 million deaths worldwide in 2024.[1] Metastasis is reported to account for over 90% of cancer-related mortality.[2] Once primary cancer cells begin to metastasize, surgical interventions become increasingly complex, and effective pharmacological treatments specifically targeting metastatic diseases remain unavailable.[3] Notably, lung cancer has the highest incidence and mortality rate worldwide among malignant tumors.[1] This aggressive cancer can metastasize to various organs, including bone,[4] brain,[5] and liver.[6] Clinical statistics further reveal that bone is the most frequent site of lung cancer metastasis.[7] The bone microenvironment is a complex and dynamic niche, characterized by a network of fenestrated capillaries that facilitate nutrient and oxygen exchange. In addition, it features a specialized bone matrix composed of collagen and hydroxyapatite, which provides structural support and serves as a reservoir for growth factors. Various bone cells, including

[a] *Department of Applied Biology and Chemical Technology, The Hong Kong Polytechnic University, Hung Hom, Kowloon, Hong Kong SAR, China. E-mail: xin.zhao@polyu.edu.hk*
[b] *The Hong Kong Polytechnic University Shenzhen Research Institute, Shenzhen, China*
[c] *Department of Electrical and Electronic Engineering, The University of Hong Kong, Hong Kong SAR, China*
[d] *State Key Laboratory for Manufacturing Systems Engineering, Xi'an Jiaotong University, Xi'an, China*
[e] *Research Institute for Intelligent Wearable Systems, The Hong Kong Polytechnic University, Hung Hom, Kowloon, Hong Kong SAR, China*

osteoblasts, osteoclasts, and osteocytes, play critical roles in bone remodeling and maintenance.[8] Additionally, this microenvironment is enriched with signaling molecules (*e.g.*, bone morphogenetic proteins (BMPs), transforming growth factor-βs (TGF-βs)) and cytokines (*e.g.*, interleukins (ILs), tumor necrosis factor alpha (TNF-α)) that can significantly influence the behavior of metastatic tumor cells, promoting processes such as cancer quiescence, escape from dormancy, and tumor invasion.[9] The interplay among these cellular components creates a unique microenvironment that can either support or impede cancer progression. To elucidate the mechanisms underlying cancer metastasis, the classic "seed and soil" hypothesis has been proposed.[10] This hypothesis postulates that primary cancer cells (seed) preferentially colonize specific organ sites (soil) where the microenvironment is conducive to metastasis. Recent research also attributes this organotropism to the formation of the pre-metastatic niche, which modifies the local environment of target organs to create conditions favorable for the colonization and proliferation of primary cancer cells.[11] Therefore, a comprehensive understanding of the interactions between primary tumor cells (seed) and the bone microenvironment (soil), the behaviors of metastatic tumor cells as well as the underlying mechanisms, is crucial for identifying targets for early diagnosis and developing effective therapeutic strategies for lung cancer bone metastasis.

Current research approaches for studying cancer metastasis primarily include *in vitro* cell culture and animal models. *In vitro* cell culture involves culturing cells with collected supernatants or using transwell systems. However, these methods lack physiological conditions and dynamic stimulations.[12] For animal models, daily injections of normal culture medium (control group) and tumor-conditioned medium (experimental group) are used to construct bone metastasis models.[13] However, predicting or controlling metastatic sites remains a significant challenge in such models.[14] In recent years, organ-on-a-chip systems have emerged as a novel platform,[15,16] offering significant advantages over traditional cell culture systems by effectively replicating vital cell niches and physiological conditions *in vitro*. These microfluidic chip systems contain hollow vessel microchannels lined with human-derived cells, establishing organ-specific tissue–tissue interfaces and simulating intricate interactions between various tissue types. Moreover, these systems replicate essential physiological microenvironments (*e.g.*, fluid flow) crucial for accurately modeling human organ-level pathophysiology.[17,18]

For example, organ-on-a-chip systems have been increasingly used to study cancer bone metastasis and have successfully modeled key characteristics of the bone microenvironment, such as specific cellular composition and biochemical signaling.[19–22] However, most current models use simple parallel channel designs, representing an oversimplified vascular structure that neglects the highly vascularized and multiscale vessel structure of bone tissue.[23] This simplification may limit the accurate simulation of nutrient exchange, oxygen delivery, cell migration, and the establishment of metastatic niches.[24] Thus, such parallel channel systems cannot accurately recapitulate these gradients and spatial heterogeneities, which are crucial for realistic modeling of tumor cell colonization, dormancy, and invasion, thereby affecting the physiological relevance and reliability of cancer bone metastasis models.[21] Inspired by leaf venation and circulatory systems, our previous work demonstrated that the leaf-vein engraved membrane can upregulate angiogenesis-related gene expression in endothelial cells, supporting the construction of highly vascularized tissue with a multiscale vascular network.[25] Additionally, we showed that the leaf vein chip can mimic the *in vivo* complex architectures of the human cardiovascular system and facilitate the formation of vascularized liver and bone organoids, providing a proof-of-concept for organ-specific metastasis studies.[26] In the present work, rather than claiming to fully recapitulate the entire metastatic cascade, we focus on leveraging this hierarchical, endothelialized microfluidic platform as a controllable *in vitro* microenvironment for investigating how uniform and stable shear stress and passive hierarchical flow distribution impact cell migration and spatial organization within a bone-mimetic chamber. This approach enables quantitative studies of cell behavior in response to well-defined biomechanical and structural cues. Furthermore, the underlying mechanisms of metastasis within such biomimetic chip systems remain largely unexplored. Therefore, we hypothesize that employing the leaf-chip platform as a controllable, endothelialized microfluidic environment, with a demonstration of a bone-mimetic chamber, can serve as a useful tool for mechanistic studies of tumor cell migration, dormancy, and reactivation under physiologically relevant flow conditions, rather than as a direct simulation of the entire metastatic process.

Here, we propose a microfluidic chip with a leaf vein structure, incorporating bone microenvironments within chambers and a vascular network within channels (Fig. 1). This design provides a controllable and uniform endothelialized environment with hierarchical flow, allowing us to dissect how passive flow distribution and endothelial interactions affect tumor cell migration and fate within a bone-like setting.[27] Rather than modeling the full metastatic cascade, the bone module serves as a demonstration unit for investigating specific microenvironmental influences. In this leaf vein chip system, bone stromal cells (HS-5), osteoclast precursor cells (THP-1), and endothelial cells (HUVECs) were utilized to recreate distinct aspects of the bone microenvironment. HS-5 cells play a central role in supporting hematopoiesis, regulating immune cell activity and establishing a niche for metastatic tumor cell dormancy and reactivation.[28] THP-1 cells can differentiate into osteoclasts, thereby modeling the "vicious cycle" niche and enabling osteoclast-mediated modulation of the tumor microenvironment.[29] HUVECs were incorporated to establish the vascular niche, which facilitates vascular–tumor and vascular–stromal interactions, as well as the formation of perfusable, functional microvessels.[26] To simulate metastatic interactions, the conditioned medium of A549 lung cancer cells (seed) enriched with cytokines was used to modify the distant bone microenvironment (soil). As a proof of concept, the leaf

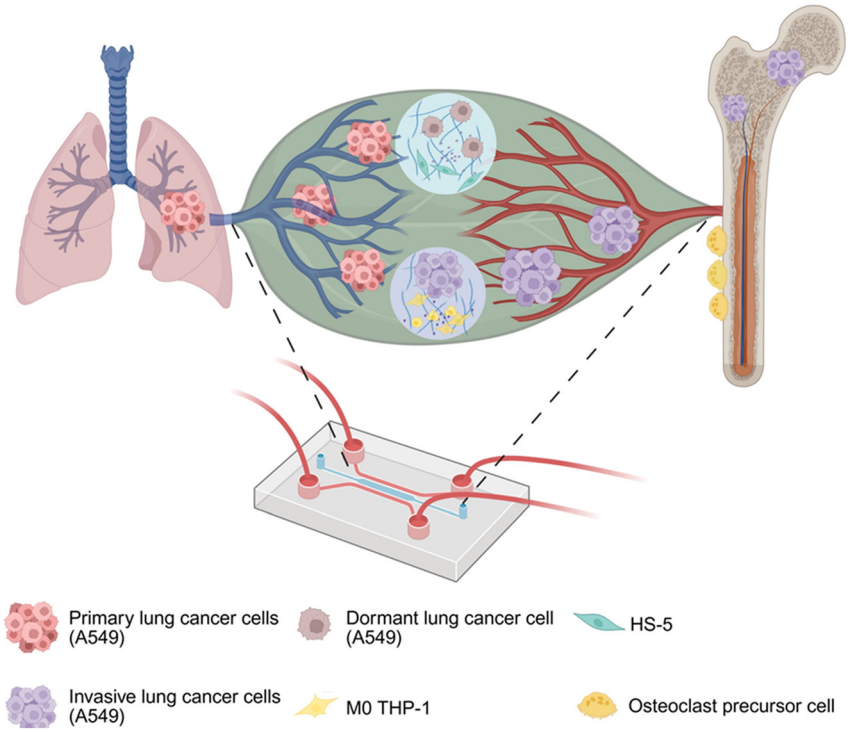

Fig. 1 Schematic diagram showing the application of the leaf vein microfluidic chip to lung cancer bone metastasis. Different cellular compositions, extracellular matrices, and biochemical signals are recapitulated to mimic tumor dormancy and invasion in the leaf vein chip system.

chip system was maintained and evaluated for two weeks. Cell morphology, related gene expressions of tumor cells, and the underlying mechanisms were systematically analyzed. Our results demonstrate that the hierarchical channel configuration enables stable shear and spatial control of cell migration and distribution, while the bone-mimetic chamber supports quantitative analysis of tumor cell dormancy and reactivation in response to microenvironmental changes. This *in vitro* system provides a versatile and mechanistically tractable platform for investigating how microenvironmental structure and flow impact cancer cell behavior in a bone-mimetic context, offering insights for future pathological analysis, drug screening, and microenvironment-targeted therapeutic development.

Experimental section

Design and fabrication of the leaf vein chip

CAD files of the leaf vein pattern and other patterns were modified by AutoCAD software (Autodesk, USA) based on previous research results.[25,26] The design modifications allowed for the incorporation of inlets connected to straight or Y-shaped channels, outlets, and chambers into the leaf vein pattern, enabling the creation of a more versatile and functional microfluidic chip system. A photomask was fabricated for the subsequent photolithography. Silicon wafers with 150 μm depth were made by SU-8 micropatterning. Then, polydimethylsiloxane (PDMS; Sylgard 184, Dow Corning) prepolymer solution and the curing agent were mixed in a ratio of 10 : 1 (w/w), degassed under vacuum to remove air bubbles, and cast onto the pre-treated silicon wafer for additional vacuum defoaming. Once all bubbles were eliminated, the silicon wafer was placed in an 80 °C oven to cure the PDMS precursor. After curing for over four hours, the PDMS was demolded from the silicon wafer and sandwiched between two polymethyl methacrylate (PMMA) layers. These PMMA layers with 1.5 mm diameter holes were secured to the PDMS by screws and nuts. The inlet and outlet with 2 mm diameter holes on PMMA layers were inserted with 23G steel needles and connected to a 10 mL syringe using polytetrafluoroethylene (PTFE) tubing with an inner diameter of 0.60 mm. This assembly ensured tight sealing and facilitated fluid flow within the microfluidic chip system.

Perfusion experiments within the leaf vein chip

To characterize the medium perfusion, dye solutions were utilized. Prior to the perfusion experiments, the leaf vein chip was sealed, immersed in deionized water, and subjected to vacuum to eliminate all air bubbles. Subsequently, blue and red dye solutions were injected at a flow rate of 20 μL min^{-1} through a Y-shaped inlet using a 10 mL syringe and syringe pump (Longer Pump, China).[26] Images of the dye perfusion were captured at predetermined time points.

To assess the medium perfusion between the channels and chambers, fluorescein isothiocyanate (FITC)-dextran (70 kDa, Sigma-Aldrich) was used. Prior to the perfusion experiments, 2 μL of 6 mg mL^{-1} fibrinogen (341573, Sigma-Aldrich) was mixed with 2 μL of 6 U mL^{-1} thrombin (T4648, Sigma-Aldrich). A 2 μL aliquot of the resulting mixture was

then added to each chamber of the microfluidic chip. Following the injection and crosslinking of the fibrin hydrogel in the chip chambers, the FITC-dextran solution was introduced into the channels. The perfusion was recorded immediately using fluorescence microscopy (TI-E ECLIPSE, Nikon). Fluorescence images were captured at predetermined time points to observe the communication of the medium between the chambers and channels.

The flow velocity in the microfluidic chips was analyzed by particle image velocimetry (PIV) analysis. Microbeads (10 μm) suspended in PBS were perfused into different microfluidic chips at a flow rate of 20 μL min^{-1}. The movement of microbeads in channels was captured at a frame rate of 20 frames per s. The flow field was analyzed using PIVlab and the average velocity was calculated through MATLAB software. The velocity was determined by measuring the displacement of the microbeads over time. In addition, microbeads at a density of 2×10^6 particles per mL were perfused into the microfluidic chips for counting to simulate the distribution of tumor cells in each chamber.

Modelling and flow analysis

To simulate fluid flow within the chambers and channels of the leaf vein chip, the CAD files of the leaf vein pattern and other patterns were processed using Gambit software to generate MESH files, which were then imported into ANSYS Fluent software (Swanson Analysis Systems, USA) for computational fluid dynamics (CFD) analysis. During the simulation, the chambers were designated as blank regions to represent the presence of 3D fibrin hydrogels, as used in the perfusion experiments. Using ANSYS Fluent, the velocity and stress distributions within the channels and chambers of the leaf vein chip were simulated.[30]

Formation of the vascular network in the leaf vein chip

Before cell perfusion, a coating was prepared on the leaf PDMS and the bottom PMMA cover to promote cell adhesion. A solution of 1 mg mL^{-1} fibrinogen was dissolved in PBS and applied to the surfaces of both the PMMA cover and the PDMS leaf chip. The coated PDMS and PMMA were incubated for 24 hours. After incubation, the fibrinogen solution was carefully decanted, and the surfaces were left to dry until no liquid remained. The presence of a white precipitate on both the PDMS and PMMA confirmed successful fibrin coating.

To establish a functional vascular network within the microfluidic chip, HUVECs (Zhongqiaoxinzhou Biotech, China) at passages 6–8 were utilized to create a healthy endothelium. To enable visualization and tracking of cell behaviors and distribution, green fluorescent protein (GFP)-labelled HUVECs and red fluorescent protein (RFP)-labelled HUVECs were used. Subsequently, 6 U mL^{-1} thrombin was diluted as the crosslinking reagent with an endothelial cell medium (ECM, Sciencell). A separate solution of 6 mg mL^{-1} fibrinogen was prepared in Dulbecco's phosphate buffered saline (DPBS, Biosharp). HUVECs were harvested *via* trypsinization and centrifuged to achieve a concentration of 1×10^7 cells per mL. After the medium was decanted, the cells were mixed with the 6 U mL^{-1} thrombin solution. For each chamber, 2 μL of the thrombin solution was mixed with 2 μL of the fibrinogen solution, and 2 μL of the resulting mixture was introduced into the chamber. The seeded PDMS was then incubated for 10 minutes to allow for the gelation and stabilization of the fibrin–cell matrix. Finally, the entire PDMS was assembled by enclosing the leaf PDMS with the coated PMMA and was subjected to perfusion culture for 3 days, until tube formation was observed.

After observing tube formation within the chambers, a suspension of HUVECs at a cell density of 1×10^7 cells per mL was injected into the leaf vein chip. To ensure thorough cell distribution, the emerging HUVEC suspension was collected and re-injected 2–3 times. The leaf vein chip was then placed in an incubator to allow for cell attachment over 4 hours to allow the cells to adhere to the inner surfaces. Once HUVECs were observed adhering to one side of the leaf chip, the injection was repeated for 3 additional cycles, and the entire chip was flipped to facilitate cell attachment on the opposite side, ensuring uniform coverage of the microfluidic channels. Finally, the chip was perfused at a rate of 20 μL min^{-1} for two days, enabling the HUVECs to stretch, align, and form intercellular connections.

Tumor cell experiments

A549 cells, a non-small cell lung cancer cell line (Procell, China), were used as the primary cancer cells in this study. To simulate the tumor microenvironment, HS-5 cells (Procell, China), derived from human bone marrow and often used as bone marrow mesenchymal stem cells (MSCs), were included due to their role in tumor development and immunomodulation.[31] In addition, THP-1 cells (Procell, China), a human monocytic leukemia cell line, were utilized. When treated with phorbol 12-myristate 13-acetate (CS0001, Multi Science), THP-1 cells can differentiate into macrophage-like cells (M0 THP-1), which can be further induced into osteoclast precursors and osteoclasts *in vitro* for the study of bone resorption and osteoclastogenesis. All cell types were cultured in Dulbecco's modified Eagle medium (DMEM, Gibco) supplemented with 100 U mL^{-1} of penicillin and streptomycin, and 10% v/v fetal bovine serum (FBS, Gibco) under humidified conditions at 37 °C with 5% CO_2. To label and track cell behaviors and distributions, specific fluorescent markers were employed. HS-5 cells and M0 THP-1 cells were labeled using CellTracker Blue CMAC dye (C2110, Thermo Fisher) and Violet BMQC dye (C10094, Thermo Fisher), respectively. Moreover, GFP-labelled A549 cells were also used to track the tumor cell behaviors.

To obtain tumor conditioned medium (CM), A549 cells were grown to 80% confluence and incubated in serum-free medium for 24 hours. After incubation, the CM was collected and filtered using a 0.22 μm sterile filter (Sorfa, China), and

10% FBS was added to ensure adequate nutrients. The resulting CM was stored at −20 °C for future use.

To assess cell viability within the leaf chip, live/dead staining was performed. Different cell types encapsulated in the hydrogel were injected into the chambers prior to chip assembly. Once the leaf vein chip was assembled, the encapsulated cells were stained with a live/dead assay kit (Abbkine, China) following the manufacturer's guidelines to visualize live and dead cells within the hydrogel.

Flow cytometry analysis

To assess tumor dormancy in the coculture with HUVEC and HS-5 cells, an off-chip cell cycle analysis was conducted using a flow cytometer (BD, USA). In brief, HS-5 and HUVEC cells were cultured at a density of 1×10^7 cells per mL in fibrin hydrogel within the lower well of a 0.22 μm transwell (NEST, China) for 3 days to facilitate the formation of vascular structures. They were then pretreated with or without tumor conditioned medium for 24 hours to simulate different microenvironmental conditions. Subsequently, A549 cells, at a density of 5×10^5 cells per mL, were seeded either in a 2D plate as a control group or in the upper insert of the transwell. After 24 hours of incubation, A549 cells from all groups were harvested and stained using a cell cycle kit (Elabscience, China) following the manufacturer's instructions. Modfit LT 3.0 software (Verity Software House, Topsham) was used to analyze the data.

Immunofluorescence staining

To evaluate the vascularization characteristics, the assembled leaf vein chip was cultured for 4 days and then washed with sterilized PBS to remove the cell culture medium. The vascular structures were fixed by 4% paraformaldehyde (PFA, Sigma-Aldrich) overnight at 4 °C. For cell permeabilization and blocking of non-specific binding sites, a solution containing 0.5% Triton X-100 (Triton X-100, Beyotime Biotechnology) and 3% bovine serum albumin (BSA, Beyotime Biotechnology) was applied for 2 hours at room temperature. Subsequently, the chip was incubated overnight at 4 °C with a mouse anti-CD31 antibody (1 : 100, Abcam) diluted in 1% BSA. Following primary antibody staining, the chip was incubated for 2 hours at room temperature with a goat anti-mouse IgG secondary antibody conjugated with Alexa Fluor 488 (1 : 1000, Abcam), also diluted in 1% BSA. Finally, the leaf vein chip was stained with phalloidin conjugated to Alexa Fluor 647 (1 : 500, Yeasen) to visualize F-actin (cytoskeleton) and DAPI (1 : 1000, Yeasen) for the nuclei identification. To evaluate endothelial integrity and response, VE-cadherin and KLF2 were stained with rabbit anti-VE-cadherin antibody (1 : 500, Proteintech) and rabbit anti-KLF2 antibody at 4 °C overnight (1 : 500, CST), respectively. Goat anti-rabbit IgG conjugated with Alexa Fluor 488 (1 : 500, Abcam) was used as a secondary antibody. DAPI (1 : 1000, Yeasen) was used to identify cell nuclei.

To evaluate tumor dormancy, Ki67, a cellular proliferation marker, was stained with rabbit anti-Ki67 antibody (1 : 500, Proteintech) at 4 °C overnight. Goat anti-rabbit IgG conjugated with Alexa Fluor 647 (1 : 500, Abcam) was used as a secondary antibody. DAPI (1 : 1000, Yeasen) was used to identify cell nuclei. Ki67 was a cellular proliferation marker, with positive cells typically present in the G1, S, G2, and M phases of the cell cycle, while negative cells are usually in the G0 phase. The calculation was Ki67-positive percentage (%) = (number of Ki67-positive tumor cells/total number of tumor cells) × 100.

To assess tumor invasion ability, cortactin, a marker of invadopodia formation, was stained using a rabbit anti-cortactin antibody (1 : 500, Abcam) at 4 °C overnight. Following primary antibody incubation, a goat anti-rabbit IgG secondary antibody conjugated with Alexa Fluor 647 (1 : 500, Abcam) was applied at room temperature to enable fluorescence detection. DAPI (1 : 1000, Yeasen) was used as a nuclear counterstain to facilitate cell identification. The mean fluorescence intensity was measured using ImageJ.

Human cytokine array characterization

To characterize the cytokine secretion from the leaf chip system, perfused media from the leaf vein chip were collected for 5 days. One milliliter of the collected media was loaded onto each membrane of a human cytokine array kit (RayBiotech, USA) and processed according to the manufacturer's protocol. The cytokine level was quantified using the Protein Array Analyzer plugin in ImageJ software.

RT-qPCR evaluation

Osteoclast differentiation, a critical activity associated with bone metastasis, was selected as the key parameter to evaluate cell differentiation within fibrin hydrogels. THP-1 cells were first differentiated into macrophage-like cells by treatment with phorbol 12-myristate 13-acetate (PMA) for 48 hours. Subsequently, tumor conditioned medium (CM), along with 100 ng mL^{-1} receptor activator of nuclear factor kappa-B ligand (RANKL, PeproTech) and 100 ng mL^{-1} macrophage colony-stimulating factor (M-CSF, PeproTech), was applied for 5 days in 6-well plates to induce osteoclast formation, following previously described protocols.[32] Then, RNA was extracted according to the manufacturer's instructions (Tolobio, China). The expression levels of osteoclast differentiation-related genes of THP-1 cells were assessed using RT-qPCR analysis (Bio Rad, USA). After the perfusion culture experiment, the fibrin hydrogels were harvested from the chambers of the leaf vein chip. The fibrin hydrogels in the three leaf vein chips were used as one sample. After RNA was extracted, the expression levels of dormancy-related and osteoclast differentiation-related genes were assessed using RT-qPCR analysis. The primers for the target genes are listed in Table S2 (SI).

Statistical analysis

Each experiment was performed in triplicate unless otherwise specified, and the results were presented as mean ± standard deviation. GraphPad Prism software (GraphPad Software, USA)

was used to investigate statistical comparisons between two data sets using the *t*-test. Statistical significance was defined as a difference at $*p < 0.05$, $**p < 0.01$, or $***p < 0.001$.

Results and discussion

Characterization of the leaf vein chip

Firstly, the leaf vein model, including inlets, outlets, and chambers, was designed and used to fabricate a silicon wafer mold. The primary structures of the leaf vein pattern, with a depth of 150 μm, include microchannels ranging from 20 μm to 350 μm and six chambers, each with a diameter of 2 mm, designed to load hydrogels and simulate organ spaces (Fig. 2Ai). After obtaining the silicon wafer, the PDMS layer featuring the leaf vein structure was prepared through the demolding process. Before sealing the chip, the fibrin hydrogels were loaded into the chambers. The PDMS layer was then sandwiched between PMMA layers and secured with screws to construct the final microfluidic chip, which was subsequently used for downstream experiments (Fig. 2Aii).

To evaluate the fluid diffusion in the leaf vein chip, dye solutions were injected through the inlets by a syringe pump at a flow rate of 20 μL min^{-1}. As shown in Fig. 2Bi, the blue dye solution successfully filled all channels and chambers without the presence of bubbles or leaks, indicating that the created chambers had minimal impact on the fluid diffusion within the chip system. Moreover, red and blue dyes were independently injected through two inlets. The results confirmed that the leaf vein chip can support the half-and-half perfusion mode, allowing for two distinct culture conditions to be maintained within the chambers on opposite sides of the chip (Fig. 2Bii). Before FITC-dextran perfusion, 3 mg mL^{-1} fibrin gels were loaded into the chambers of the leaf vein chip. To characterize the efficiency of the convective and diffusive transport within the leaf vein chip, the FITC-dextran solution was injected through the inlets by a syringe pump at a flow rate of 20 μL min^{-1}. After 60 minutes of perfusion, the average fluorescence intensity between chambers and channels appeared similar (Fig. 2C). This indicated that the biomimetic channels and chambers facilitated effective exchange of nutrients and metabolic waste with the cells embedded in the fibrin hydrogels.

To further investigate the flow dynamics within the biomimetic vascular network, we conducted a numerical finite-element simulation using ANSYS Fluent. The fibrin hydrogel-loaded chambers were modeled as a stiff hydrogel, assumed to resist fluid pressure without allowing liquid flow. As shown in Fig. 2Di, a high concentration of velocity was observed at the Y-shape inlets. Once the liquid entered the main channel of the leaf vein, the velocity distribution across the channels and around the chamber was stable. In addition, the pressure distribution from the inlet to the outlet exhibited a gradual decrease and was symmetric across the corresponding parts of the leaf vein structure. Furthermore, the simulation result demonstrated that the hydrogel-loaded chamber had no significant effect on the surrounding pressure distribution (Fig. 2Dii). These results suggested that the leaf-inspired microfluidic chip can support the stable transport of liquid and half-and-half perfusion mode, making it suitable for applications requiring controlled flow conditions.

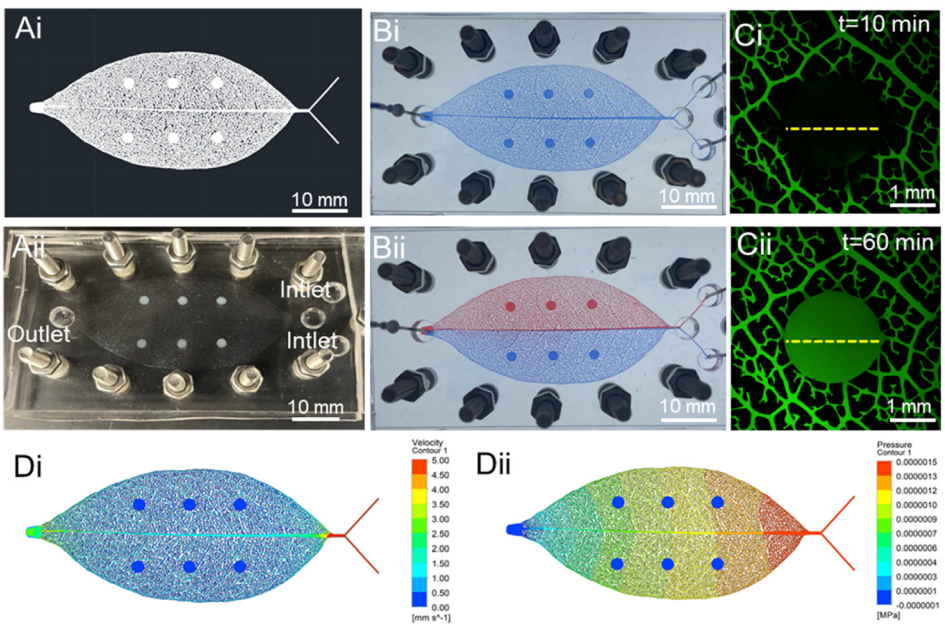

Fig. 2 Design and application of the biomimetic leaf vein microfluidic chip. A) General overview of the leaf vein microfluidic chip. (i) CAD image. (ii) Macroscopic view of the leaf vein chip with fibrin hydrogels loaded in chambers. B). Representative images of dye perfusion in the leaf chip system. (i) Uniform medium distribution in the entire chip. (ii) Half-and-half perfusion demonstrating the stable laminar flow. C) FITC-dextran perfusion through the biomimetic vascular system integrated with six chambers filled with fibrin hydrogels at (i) 10 min and (ii) 60 min. D) Fluid simulation and modelling of the chip. (i) Velocity distribution and (ii) pressure distribution in the leaf vein microfluidic chip with hydrogels in chambers.

To characterize the flow velocity inside the microfluidic network of the leaf chip, particle image velocimetry (PIV) was employed to trace the movement of microbeads. Microfluidic chips with different branching configurations, including no branch, single branch, three branches and grid, were utilized to compare the fluid dynamics performance. The channel width of these chips was the same as the average diameter of the channels in the leaf vein chip (150 μm). The first three branching configurations are migration chips simplified according to the size of the leaf vein chip, primarily consisting of chambers and connecting channels.[33] The grid structure also represents a common microvascular network that has been studied to investigate the impact of internal flow patterns on vascular disease pathology.[34] In addition, Fang *et al.* fabricated grid patterns with channel widths ranging from 150 μm to 30 μm and compared their ability to induce endothelial cell differentiation to that of the leaf vein pattern. The expression of angiogenesis marker genes (PECAM-1, CDH5) and tip cell-related genes (KDR, Dll4) increased as the channel width decreased in the grid patterns, while the gene expression in the leaf vein pattern was the highest among all groups. This indicated that channels of different diameters may contribute to the regulation of angiogenesis and tip cell/stalk cell differentiation.[25] In this study, we analyzed the velocity field distribution of different microfluidic chips at the entrance of each chamber across different microfluidic chips, as well as the distribution of microbeads in each chamber to simulate the perfusion of tumor cells into the chamber of different microfluidic chips. As shown in Fig. 3A, the maximum flow velocity for the no branch, single branch, and three branches could reach 0.6 mm s^{-1}, with an average velocity of approximately 0.25–0.30 mm s^{-1}. The distribution of velocity uniformity in the no branch and single branch groups was uneven, while the three branches' group exhibited improved velocity uniformity due to the increased number of branches. Although the grid structure exhibited a uniform velocity distribution, it had the lowest maximum velocity (0.15 mm s^{-1}) and average velocity (0.07 mm s^{-1}). The leaf vein chip demonstrated an increase in flow velocity, with a maximum velocity of 0.25 mm s^{-1} and an average velocity of 0.10 mm s^{-1}. The velocity field in the leaf vein chip was uniform and close to the simulation results of velocity distribution (Fig. 2Di), attributed to its hierarchical structure. The fluid flow was smoother in wider channels, leading to an increased flow rate. In contrast, fluid flow was restricted in narrower channels, resulting in a natural decrease in flow rate. This characteristic simulates the adaptability of natural blood vessels, which adjust flow rates by altering diameter and branching patterns to ensure effective and stable delivery under varying physiological conditions. We further developed various 2D simplified models of these microfluidic chips to analyze the velocity and pressure distribution (Fig. S1, SI). By increasing the number of branches, the velocity distribution at the inlet and outlet of the chamber could be stabilized. For pressure distribution, the no branch group has a relatively low pressure drop (23.96 Pa) due to the merged channels with the increased diameter. Comparing the remaining groups, it could be observed that increasing the number of branches could also result in a lower pressure drop

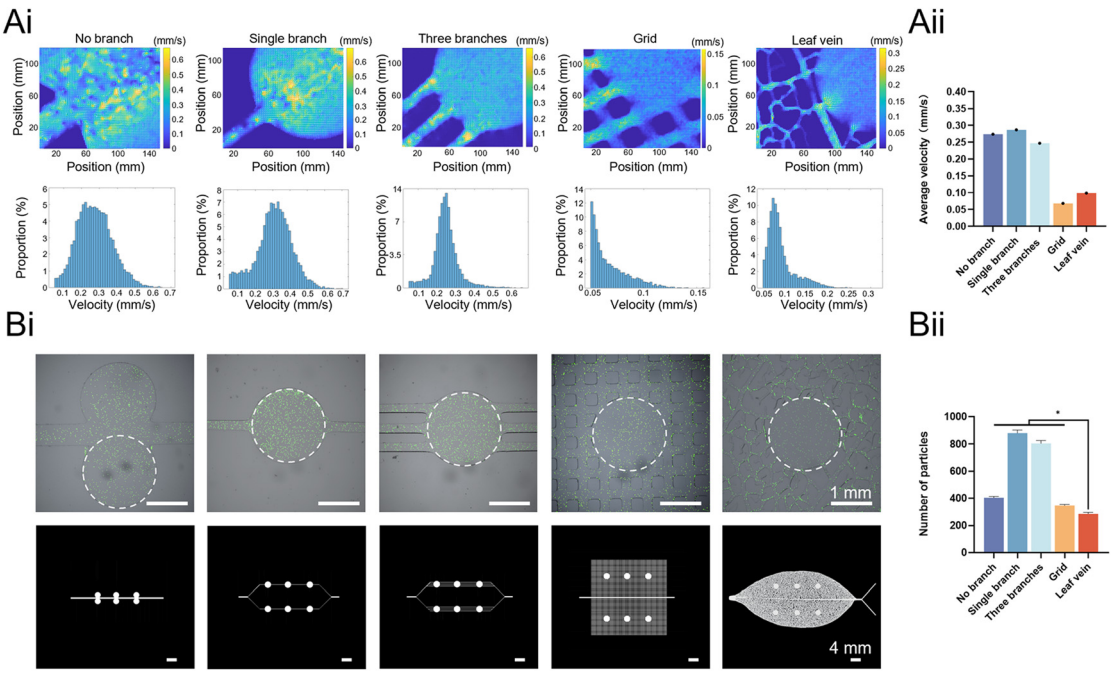

Fig. 3 Velocity characterization of the leaf vein chip and other microfluidic chips with chambers and different degrees of branching. A) The velocity profiles acquired from PIV measurement in the microfluidic chips. (i) Velocity magnitude and distribution. (ii) Average velocity. B) Representative images of fluorescent microbeads perfused into microfluidic chips. (i) Distribution of fluorescent microbeads. (ii) Number of microbeads in each chamber. The differences are statistically significant when p values are below 0.05 (*), 0.01 (**), and 0.001 (***).

of the leaf vein chip (116.02 Pa) compared to the single branch group (322.13 Pa) and the three branches' group (183.03 Pa). Although the pressure drop of the leaf vein chip was not as low as that of the grid group (18.87 Pa), the leaf vein chip could yield uniform shear and provide a stable velocity field, which could be observed from the simulation models. To further quantify velocity uniformity in the chamber, we calculated the coefficient of variation (CV) for flow velocity in the chamber across different microfluidic designs (Table S1, SI). The leaf vein chip exhibited a smaller CV value (27.38%) compared to the no branch group (41.30%), the single branch group (30.39%) and the grid group (29.91%), indicating a more uniform velocity distribution, supporting the stabilizing effect of the hierarchical network. This quantitative result was consistent with the simulation and PIV data. For the design of channel geometry, increasing the number of branches and changing the diameter of channels could be effective ways to achieve lower pressure drop. Other factors such as velocity, velocity uniformity, and shear distribution could be optimized based on Murray's law to further adjust the diameter and the branching angle for application. In addition, we perfused fluorescent microbeads into microfluidic chips, and the density of microbeads was consistent with the cell density of tumor cells used in subsequent perfusion experiments. We found that the number of microbeads entering the single branch and three branches' group was the largest, while the number of microbeads was fewer in the no branch group. This discrepancy may be attributed to the instability of lateral flow, which caused microbeads to enter the chamber in an erratic manner. In the grid and leaf vein structures, the number of microbeads entering each chamber was only 40% and 30% of that in the single branch group, respectively (Fig. 3B). This indicated that the single branch structure exhibited lower selectivity and filtration efficiency. Conversely, the leaf vein structure resulted in fewer microbeads entering the chambers, suggesting a degree of selective entry or "filtration". It should be noted that this observation is based on relative microbead counts and should be interpreted as a qualitative, rather than mechanistically proven, filtration effect. No direct mechanistic or size-dependent validation was performed in this study. Additionally, microbeads that do not enter the chamber preferred small tertiary channels to relatively larger secondary channels due to the fluid shear force, which is in accordance with previous studies.[35] These results indicate that the leaf vein structure can promote a more stable flow field and a qualitative filtration effect for the perfusion of tumor cells into the chambers. The filtration property, as assessed by microbead entry, is an indirect observation and remains to be validated by further mechanistic studies.

Construction of the vascular network in the leaf vein chip system

To construct the entire vascular network in the leaf chip system, we performed the sequential cell seeding procedures according to the timeline outlined in Fig. 4A. The self-assembled vascular network within chambers was constructed first. The fibrin hydrogel encapsulated with GFP-HUVECs at 1×10^7 cell per mL was injected into the chambers on day 1 (Fig. 4Bi), and then the PDMS layer and PMMA layers were assembled for perfusion culture. During the initial two days of culture, GFP-HUVECs began to stretch and establish intercellular connections. On day 3, GFP-HUVECs had formed a three dimensional (3D) branched microvascular network within the chamber (Fig. 4Bii). Then, RFP-HUVECs at 1×10^7 cell per mL were introduced into the channels in two sequential injections to ensure endothelial cells adhered to both the upper and lower surfaces of the microfluidic channels (Fig. 4Biii). After a 4 hour adhesion period for the RFP-HUVECs, the entire system was perfused with ECM for two days at 20 μL min^{-1} to promote cell adhesion and spreading. As shown in Fig. 4Biv and Movie S1 (SI), GFP-HUVECs within the chambers were successfully connected with RFP-HUVECs in channels, forming an integrated vascular network. This suggested that leaf vein chips could successfully mimic the *in vivo* architecture of the human vascular systems that connect the organs. The live/dead staining of HUVECs in the chamber indicated that the processes of chip assembly and dynamic perfusion did not affect cell viability (Fig. 4C). CD31 and F-actin immunofluorescence staining revealed the successful construction of the self-assembled vascular network within the chambers (Fig. 4Ciii and iv). Moreover, the cross-sectional view of CD31 and F-actin staining showed the formation of lumen structures in the main channel, as well as in middle part and edge part of the leaf chip (Fig. S2A, SI). The oriented cell nucleus also indicated that HUVECs could align along the microfluidic channels at a flow rate of 20 μL min^{-1} (Fig. S2B, SI). These results indicated that the leaf-inspired microfluidic chip could effectively support the dynamic culture of the endothelialized microfluidic network, highlighting its potential as a novel organ-on-a-chip system.

Specialized tissue microenvironments, composed of various cellular components, play a critical role in regulating tumor cell colonization, encompassing processes such as initial seeding, dormancy, and subsequent outgrowth.[8] In our study, we set to mimic different metastatic processes of lung cancer cells from their migration through the vascular network to colonization within a vascularized bone environment. For this purpose, we further built two types of vascularized bone microenvironment within our biomimetic vascular system. We initially hypothesized that the tumor conditioned medium could influence the bone microenvironment and further impact the behaviors and expression of metastatic tumor cells. Therefore, tumor conditioned medium was used to establish the connection between the primary tumor cells and the bone environments. As shown in Fig. 4D, 5×10^6 cells per mL fibroblast-like HS-5 cells were labelled blue, which could form the network structure when co-cultured with 5×10^6 cells per mL HUVECs for 3 days. Similarly, 5×10^6 cells per mL M0 THP-1 cells were labelled purple. When co-cultured with 5×10^6 cells per mL HUVECs for 3 days, M0 induced THP-1 cells still maintained the macrophage phenotype within the vascularized system (Fig. 4E). Live/dead assay also demonstrated the high

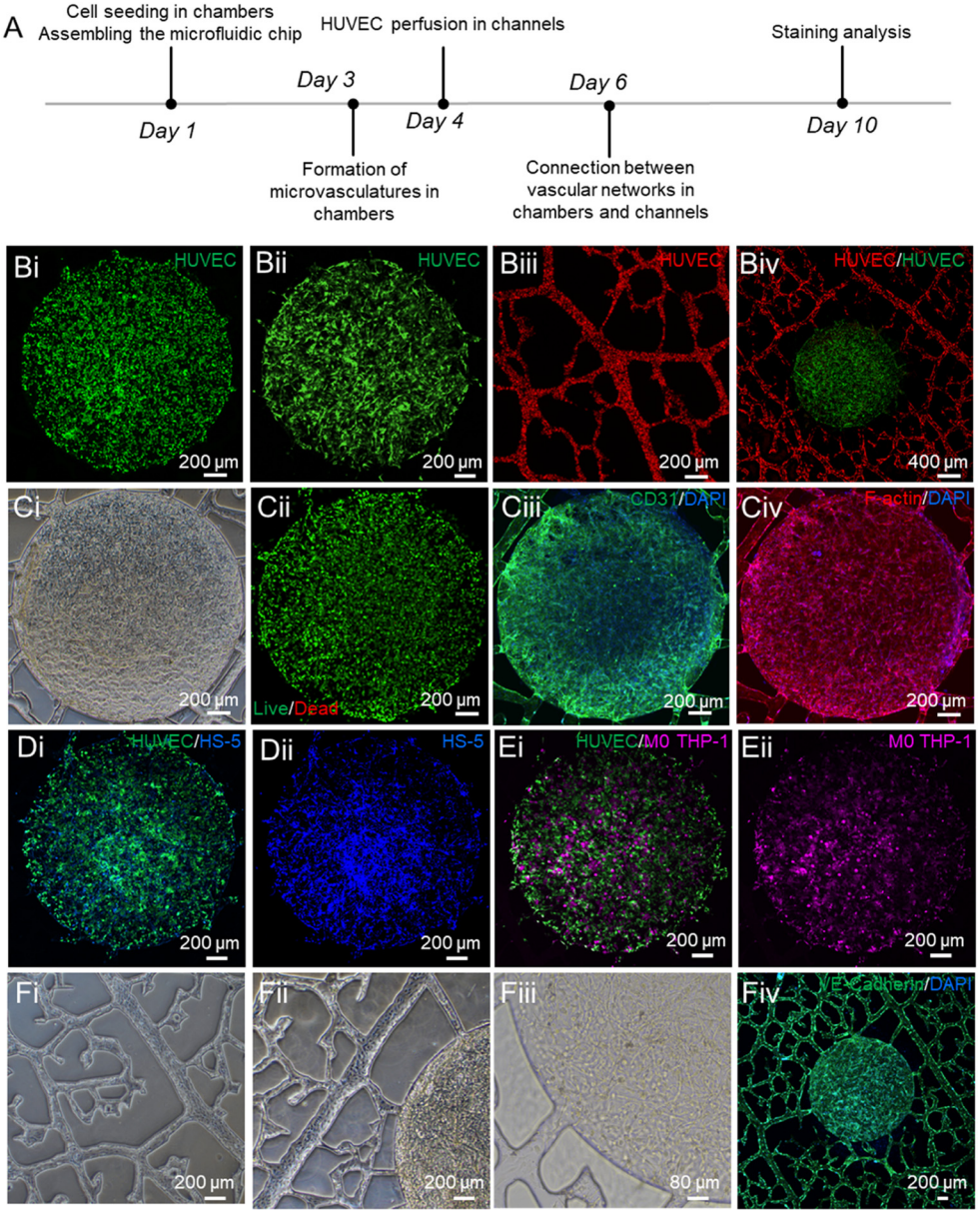

Fig. 4 Cell distribution in the vascularized bone-on-leaf-chip. A) Timeline of the vascularized leaf vein chip operation procedures. B) Formation of the vascularized bone-on-leaf-chip. (i) GFP-HUVECs were seeded in chambers on day 1. (ii) Formation of the microvascular network by GFP-HUVECs on day 3. (iii) RFP-HUVECs were introduced into the channels to construct the endothelialized microfluidic network on day 4. (iv) Connection between vascular networks in chambers by GFP-HUVECs and channels by RFP-HUVECs on day 6. C) Representative images of the vascular network in the chamber. (i) Optical microscope image of the vascular network in the chamber. (ii) Live/dead staining of HUVECs in chambers. (iii) Immunofluorescence images of the vascular network in the chamber stained with CD31 (green) and DAPI (blue). (iv) Immunofluorescence images of the vascular network in the chamber stained with F-actin (red) and DAPI (blue). D) Fluorescence images of GFP-HUVEC/cell-tracker labelled HS-5 (i) and cell-tracker labelled HS-5 (ii) in the chamber. E) Fluorescence images of GFP-HUVEC/cell-tracker labelled M0 THP-1 (i) and cell-tracker labelled M0 THP-1 (ii) in the chamber. F) Representative images of the vascular network in the leaf vein chip. (i) Optical microscope image of the vascular network in channels. (ii) Optical microscope image of the vascular network between the chamber and channels. (iii) The enlarged view of the vascular network in the fibrin hydrogel in one side of the chamber. (iv) Immunofluorescence image of the vascular network in the leaf vein chip stained with VE-cadherin (green) and DAPI (blue).

viability of cells in these two different bone environments, indicating that the processes of chip assembly and dynamic perfusion did not affect cell viability (Fig. S3A, SI). The optical microscope image and CD31 immunofluorescence staining within the channels demonstrated the successful vascularization within channels of the leaf vein chip (Fig. 4Fi and S4Ai, SI). In addition, the optical microscope image and CD31 staining at the interface between the channels and chambers demonstrated the establishment of connections between the vascularized organ and the vessel network (Fig. 4Fii and S4Aii, SI). As shown in the enlarged view of the cell-laden fibrin hydrogel in the chamber (Fig. 4Fiii), the vascular network

formed by HUVECs and HS-5 cells can be seen under a large aperture. These structures were not spherical and contained the certain interstitial space, which is similar to the morphology of the MSC-loaded fibrin hydrogel or HUVEC and MSC-loaded fibrin hydrogel in other bone marrow microfluidic chips.[21,36] The structure of the fibrin hydrogel co-assembled with HS-5 and HUVECs lacks a well-defined vascular architecture compared to the vascular networks formed by HUVECs and other fibroblast cell lines. This may be due to the limited association between the microvessels and HS-5 cells that remain embedded in the matrix during co-culture, while MSCs and HS-27A cells demonstrated a pericyte-like association with the microvessels.[37] However, HS-5 cells serve as a stable bone marrow stromal cell line due to their ease of manipulation *in vitro*, which is capable of reliably reproducing the characteristics of MSCs[31] and inducing tumor dormancy.[38,39] Furthermore, the vascular structure could allow tumor cells to infiltrate into the chamber through the channels (Fig. S5A, SI). In contrast, the pure fibrin hydrogel or the fibrin hydrogel loaded with MSCs alone presented a substantial barrier for tumor cell invasion in leaf vein chips.[36] VE-cadherin immunofluorescence staining revealed the endothelial integrity in the chamber as well as between the chamber and channels in the leaf vein chip (Fig. 4Fiv). In addition, the flow applied in the leaf vein chip elicited more KLF2 expression than the static condition; both the endothelial cells in the fibrin hydrogel and in channels were activated by the shear stress generated by the dynamic culture (Fig. S6A, SI). These results indicated that the vascularized bone microenvironments within the biomimetic vascular system can effectively simulate physiological conditions to study the interactions between metastatic tumor cells and the bone microenvironments.

In vitro model of tumor dormancy

A 3D engineered soft matrix has been reported as an important regulator of tumor dormancy.[40] Fibrinogen is found around blood vessels in the bone marrow, and the fibrin hydrogel has been used to create vascularized microphysiological systems in a bone marrow-on-a-chip to construct the perivascular niche composed of endothelial cells and bone marrow stromal cells, as well as the endosteal niche composed of endothelial cells and human fetal osteoblast (hFOB) 1.19 cells.[21] Meanwhile, the cannibalization of bone mesenchymal stem/stromal cells has been shown to induce tumor dormancy in cancer cells.[41] The HS-5 bone marrow-derived stromal line has been used to model dormancy in breast and prostate cancer, and shares a surface marker (CD105, CD73, CD44 and CD90) with MSCs. Cell–cell contact with HS-5 has been reported to inhibit breast cancer cell growth,[38,39] the HS-5 conditioned medium could also alter cell cycling as manifested by more cells in the G0/G1 phase and fewer cells in the G2/M phase of MCF-7 breast cancer cells than the blank group.[39] However, endothelial cells play a dual role in regulating tumor dormancy. According to Ghajar *et al.*, a stable microvascular network maintains tumor dormancy, while new blood vessels and endothelial tip cells promote proliferative growth.[42] This duality demonstrated the complex relationship between different states and expressions of endothelial cells in tumor progression. Therefore, we first conducted off-chip cell cycle experiments to verify whether co-culture with the fibrin hydrogels loaded with HUVECs and HS-5 cells could induce changes on the cell cycle of tumor cells. These experiments were performed using a transwell system that followed the same timeline and operational procedures as the on-chip analysis. The results demonstrated that co-culture with the fibrin hydrogels loaded with HS-5 and HUVEC cells could significantly increase the percentage of A549 lung cancer cells in the G0/G1 phase (from 38% to 60%), while reducing the percentages of cells in the G2/M and S phases, compared to A549 cells cultured on a 2D plate. In addition, the G0/G1 phase of A549 dropped from 60% to 40% when the fibrin hydrogel loaded with HS-5 and HUVEC cells was treated with CM (Fig. S7, SI). To validate the dormant state of tumor cells in the vascularized bone environment consisting of HUVEC and HS-5 cells in the chamber, perfusion experiments of A549 cells were conducted following the timeline and operation procedures (Fig. 5A and B). After the vascular networks in the chambers and channels were connected on day 6, normal medium (ECM : DMEM = 1 : 1) and experimental medium (ECM : CM = 1 : 1) were perfused to construct the different pre-metastatic niches on day 7, respectively. On day 9, 1 mL A549 cell suspension at 2×10^6 cells per mL was perfused into the chambers. Then, normal medium and experimental medium were perfused at 20 $\mu L\ min^{-1}$ for 5 day dynamic culture. To evaluate the dormant state of A549 cells, Ki67 staining was performed. Ki67 is a nuclear antigen associated with cell proliferation that is expressed in the G1, S, G2, and M phases of the cell cycle, but absent in the G0 phase. The initial morphology of tumor cells entering the chambers could be observed in Fig. S8 (SI). By day 14, approximately 22% of GFP-A549 cells cultured within the HS-5 and HUVEC-loaded fibrin hydrogel were Ki67-positive (Fig. 5C and D). However, with the treatment of CM, the percentage of Ki67 positive GFP-A549 cells rose to 55% on day 14, which was consistent with off-chip cell cycle experiments. These results suggested that the vascularized bone microenvironment consisting of HS-5 and HUVEC cells could successfully induce metastatic A549 cells to enter dormancy, and CM could further reactivate the dormant state of A549 cells.

As mentioned above, the purpose of this leaf vein chip was to investigate how the modification of secreted factors from primary tumor cells responds to the overall expression of the metastatic environment during the metastatic process. Therefore, we employed a human cytokine array to narrow our focus to relevant factors. After the tumor cells entered the vascularized bone microenvironment, the culture medium was collected from day 9 to day 14. Cytokines potentially relevant to our model were screened, and their relative expression levels were determined after standardizing the total cytokine content (Fig. 5E). Notably, the expression levels of IL-6, IL-8, CCL7, EGF, MIP-3α, TIMP-1 and TIMP-2 were relatively high in the normal medium group, indicating that colonization of tumor cells had an impact on the

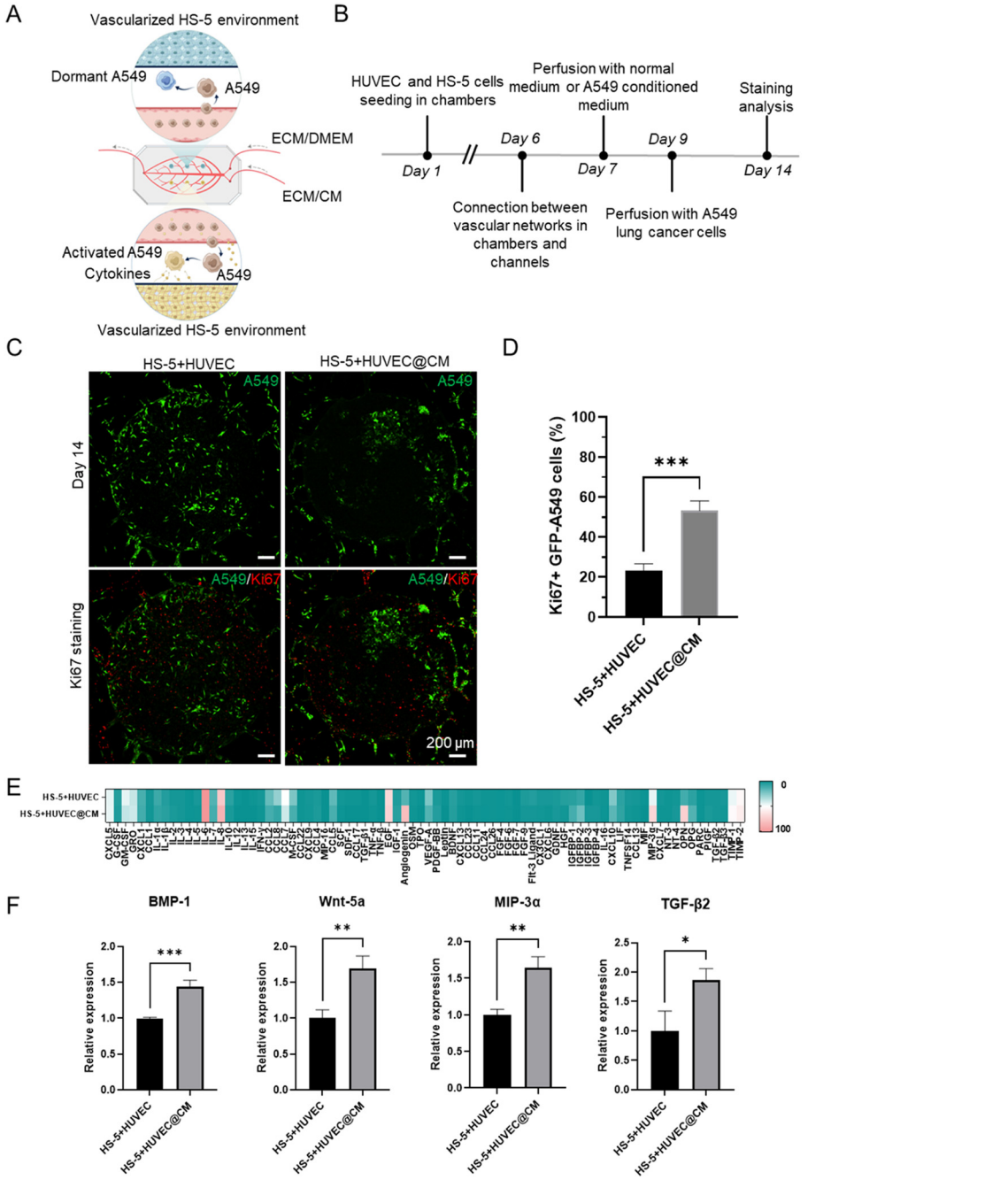

Fig. 5 Tumor dormancy in the vascularized bone-on-leaf-chip. A) Application of the vascularized bone-on-leaf-chip platform. B) Timeline of tumor cell perfusion in vascularized leaf vein chip operation procedures. C) Cell morphology for A549 in vascularized bone microenvironments on day 14. D) Quantitative analysis of Ki67 expression. E) Heatmap for human cytokine array showing relative magnitudes of secreted factors from the vascularized bone-on-leaf-chip. F) RT-qPCR of gene expression from harvested fibrin hydrogels containing HUVEC and HS-5 cells on day 14. The differences are statistically significant when p values are below 0.05 (*), 0.01 (**), and 0.001 (***).

secretion of the overall vascular bone microenvironments. Interestingly, the pro-inflammatory environments were further intensified in the CM-treated group, as evidenced by increased expression levels of angiogenin, MIP-3α and OPN, along with the decreased expression of CCL7, which are known to be critically involved in inflammation, immune cell recruitment, and angiogenesis. It should be emphasized that although changes in cytokine profiles, such as OPN elevation, may suggest bone microenvironment remodeling, our current data do not provide direct evidence of matrix or structural changes, and these conclusions remain inferential.

To further investigate the transformation process from tumor dormancy to activation, we analyzed the expression of genes associated with this transition. Based on the overall cytokine expression results above, combined with the downstream bone expression genes (*e.g.*, BMP-1, BMP-7, BMP-9,

Wnt-5a) related to tumor dormancy,[43] we aimed to screen related genes and validate the potential mechanisms. By harvesting the cell-laden fibrin hydrogels on day 14, the gene expression of the vascularized bone microenvironment in chambers was analyzed. The results revealed that CM treatment significantly increased the expression of BMP-1, Wnt-5a, MIP-3α and TGF-β2 to promote tumor reactivation. Among these factors, MIP-3α was crucial for the development of the inflammatory response and can also be regulated by CM to activate tumor cells (Fig. 5F). These findings suggested that the pro-inflammatory and signaling pathways activated by CM are key drivers of the transition from tumor dormancy to reactivation.

In vitro model of tumor invasion

Different from tumor dormancy, the "vicious cycle" niche, primarily composed of osteoclasts, exhibits properties that promote tumor invasion and trigger subsequent metastasis.[44] The role of osteoclasts has evolved from being perceived merely as bone-resorbing cells to being recognized as key regulatory factors in tumor metastasis.[45] During the metastatic process, cell differentiation (*e.g.*, monocytes/myeloid progenitor cells differentiate into osteoclast precursor cells and osteoclasts) and various cytokines play the crucial roles.[46] RAW 264.7, as a mouse-derived cell, is widely used to study primary cancer bone metastasis and can be induced by RANKL and M-CSF for osteoclastogenesis. In addition, recent studies have also validated that the A549 tumor conditioned medium can induce osteoclast differentiation. While human derived THP-1 cells are relatively immature for osteoclastic related research on bone metastasis,[43] they have been used recently for this purpose.[47] It requires PMA induction on THP-1 cells to transform into the M0 phenotype (Fig. S9A, SI), followed by osteoclast induction. In this study, we exclusively applied human derived cells to avoid potential discrepancies in gene expression analysis. We further conducted the off-chip experiments to validate the effect of CM on the induction of osteoclast differentiation of M0 THP-1. The results showed that CM induced osteoclast differentiation with comparable efficiency to RANKL and M-CSF within 5 days (Fig. S9B, SI). To further validate the invasive state of tumor cells in the vascularized bone microenvironment consisting of HUVEC and M0 THP-1 cells in the chamber, perfusion experiments of tumor cells were conducted following the timeline and operation procedures (Fig. 6A and B). After the connection between the vascular networks in chambers and in channels on day 6, normal medium (ECM : DMEM = 1 : 1) and experimental medium (ECM : CM = 1 : 1) were perfused to construct the different pre-metastatic niches on day 7, respectively. On day 9, 1 mL A549 cell suspension at 2×10^6 cells per mL was perfused into the chambers. The chambers were then perfused with normal or experimental medium at a flow rate of 20 μL min^{-1} for a 5 day dynamic culture period. Cortactin staining was used as an invadopodia marker to evaluate the invasive state of A549. The initial morphology of tumor cells entering the chambers could be observed in Fig. S10 (SI). As shown in Fig. 6C, A549 cells in the normal medium group showed an increase in cell number with less elongation on day 14. In contrast, the cell morphology of A549 in the experimental medium group on day 14 exhibited noticeable elongation and protrusion formation, which are characteristic features of the invasive state of tumor cells (Fig. 6C). The fluorescence quantitation for the cortactin expression was significantly higher in the experimental medium group compared to the normal medium group (Fig. 6D). Over-expression of cortactin has been recognized for its role in enhancing cell migration and metastatic potential. These results demonstrated that the bone environment, composed of HUVEC and M0 THP-1 cells, was altered by CM, which promoted the invasive behavior of A549 tumor cells.

The human cytokine array was analyzed using the perfused medium from day 9 to day 14. As shown in Fig. 6E, cytokines, including IL-6, IL-8, CCL5, EGF and MIP-3α, were significantly highly expressed in both the normal medium group and the experimental medium group. However, perfusion with CM significantly increased the expression of CCL5, angiogenin, CXCL5 and OPN, which are known to be critically involved in inflammation and immune cell recruitment. Nevertheless, immune cell recruitment in our model was not directly observed or quantified; the association is inferred from cytokine changes rather than real-time tracking or migration measurements.

To further investigate the mechanisms underlying tumor metastasis, we analyzed the expression of genes associated with tumor invasion and osteoclastogenesis. Based on the overall cytokine expression results above, combined with some gene expressions of osteoclastogenesis (*e.g.*, MMP-2, MMP-9, CTSK, TRAP),[43] we aimed to screen related genes and validate the potential mechanisms. By harvesting the cell-loaded fibrin hydrogels on day 14, the gene expression of cells in the vascularized bone environment were analyzed. The results revealed that CM treatment significantly upregulated the expression of CTSK and MMP-9, both of which are osteoclast differentiation-related genes implicated in promoting tumor invasion. Additionally, CCL5 expression was markedly increased in the CM group compared to the normal medium group. CCL5 is known to mediate chemotactic activity in leukocytes and to enhance tumor migration and invasion. Furthermore, VCAM-1, a molecule known to recruit leukocytes and elevate osteoclast activity, was also upregulated by CM treatment. Although our model lacks direct evidence of immune cell transmigration, VCAM-1 upregulation suggests a possible involvement in immune cell recruitment from these molecular markers (Fig. 6F). The potential mechanisms for tumor dormancy and invasion of A549 in the pre-metastatic niche are summarized in Fig. 7. When A549 cells entered the vascularized bone environment composed of HS-5 and HUVEC cells, the proliferation ability of A549 decreased, indicating a dormancy state. However, the tumor conditioned medium from the primary cancer cells could modify and regulate the bone microenvironment and the colonizing cancer cells. Under the perfusion of the tumor conditioned medium, A549 cells in the dormancy niche could be reactivated, as evidenced by an

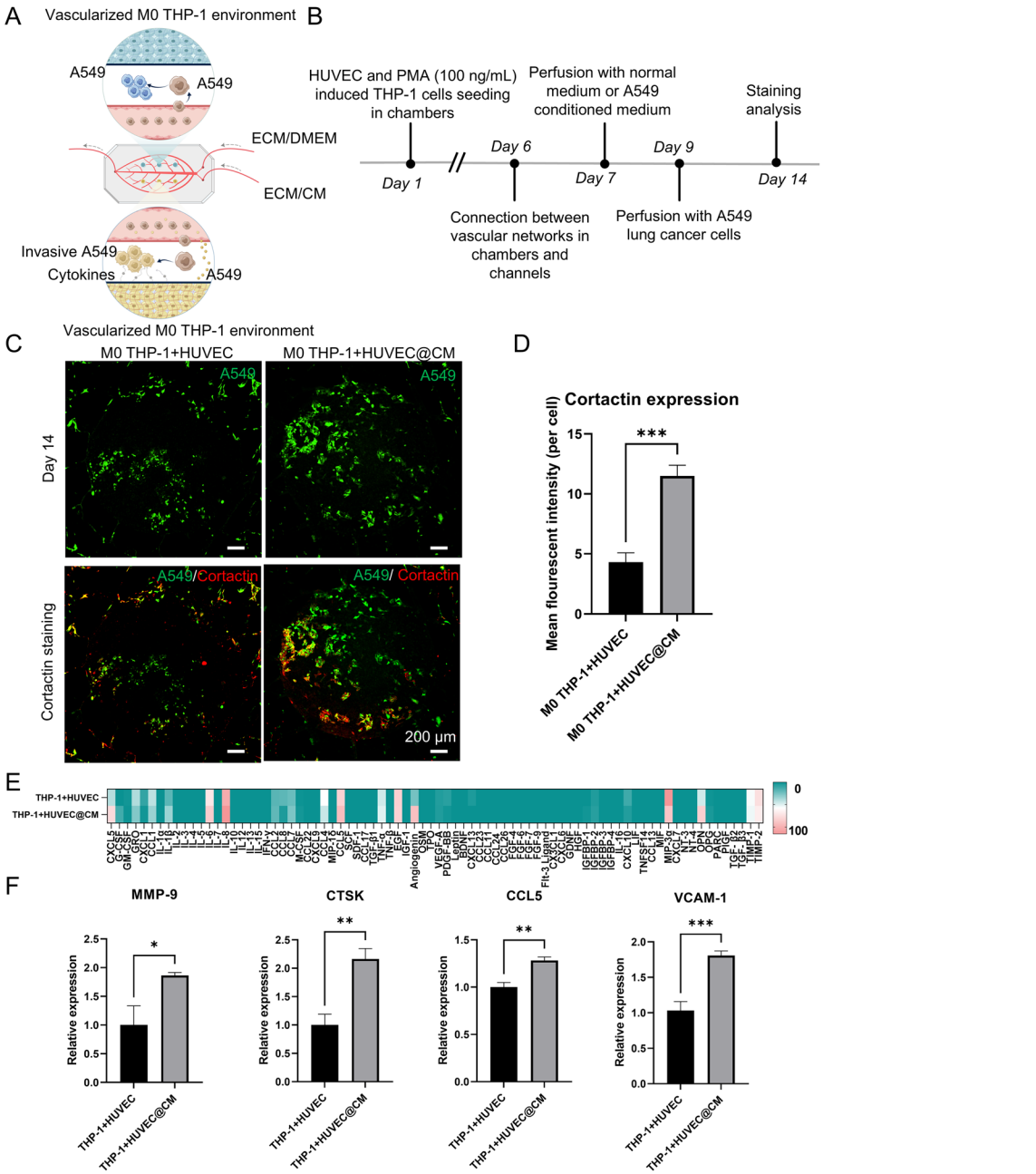

Fig. 6 Tumor invasion in the vascularized bone-on-leaf-chip. A) Application of the vascularized bone-on-leaf-chip platform. B) Timeline of tumor cell perfusion in vascularized leaf vein chip operation procedures. C) Cell morphology for A549 in the vascularized bone environment on day 14. D) Quantitative analysis of cortactin expression. E) Heatmap for human cytokine array showing relative magnitudes of secreted factors from the vascularized bone-on-leaf-chip. F) RT-qPCR of gene expression from harvested fibrin hydrogels containing HUVEC and M0 THP-1 cells on day 14. The differences are statistically significant when *p* values are below 0.05 (*), 0.01 (**), and 0.001 (***).

increase in the proportion of Ki67 positive cells, as well as a significant increase in the expression of BMP-1, Wnt-5a, MIP-3α and TGF-β2. In contrast, the bone microenvironment composed of M0 THP-1 and HUVEC cells served as a "vicious cycle" niche, promoting tumor invasion. A549 cells perfused with CM exhibited higher levels of cortactin, a marker of invadopodia formation, compared to those perfused with normal medium. By analyzing the gene expression from the perfusion medium and hydrogels extracted from the microfluidic chips, it was found that the tumor conditioned medium could promote the expression of CCL5 and VCAM-1, as well as osteoclast differentiation-related genes (CTSK, MMP-9). Overall, these results revealed the regulatory effects of the tumor conditioned medium on the interactions between primary tumor cells (seed) and the bone microenvironment (soil). They also provide new insights into the behaviors of metastatic tumor cells in distinct bone microenvironments, offering a deeper understanding of the mechanisms underlying lung cancer bone metastasis.

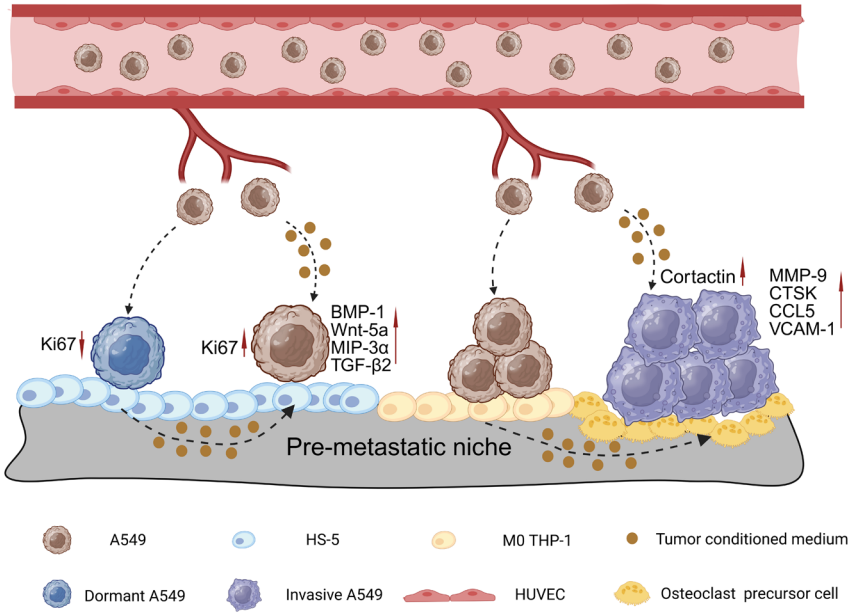

Fig. 7 Potential mechanisms for tumor dormancy and invasion of A549 lung cancer cells in the pre-metastatic niche with the treatment of the tumor conditioned medium.

In all, the biomimetic vascular system, extracellular matrix environments, and different bone niches were all incorporated into the leaf vein microfluidic system to study tumor metastasis. By analyzing cell morphology and gene expression, this platform enabled the evaluation of the core characteristics of tumor dormancy and invasion in bone metastasis. This *in vitro* platform facilitates the construction of diverse bone microenvironments under both physiological and pathological conditions, allowing for detailed analysis of the factors influencing lung cancer bone metastasis. However, there are some limitations in our study. For example, the siRNA knockdown on tumor cells can be performed for in-depth mechanistic analysis to screen and verify potential pathways involved in bone metastasis. Furthermore, tumor cells or tissues derived from patients can be utilized to simulate the authentic metastatic conditions, and drug testing could be further developed within our leaf vein chip system.

Conclusions

This study presented the application of the leaf vein chip to investigate lung cancer bone metastasis. The leaf vein microfluidic chip offers several advantages, including its ability to support a half-and-half perfusion mode, ensuring sufficient nutrient exchange, while also allowing for the creation of chambers that accommodate tissue-specific microenvironments. These chambers effectively connect with surrounding vascular networks, simulating the structure and function of human blood vessels, making it a robust and complex *in vitro* platform. This study also demonstrated the successful construction of two vascularized bone microenvironments for tumor dormancy and invasion, respectively. The key characteristics of tumor cells within these niches, along with the potential mechanisms driving their behaviors, were systematically analyzed. It should be noted that interpretations regarding bone microenvironment remodeling and immune cell recruitment are based on indirect evidence from cytokine and gene expression profiles, rather than direct observation of matrix changes or immune cell dynamics. Future work including real-time imaging and structural assays will be necessary to confirm these mechanisms. In all, this platform holds great promise for personalized diagnosis and drug screening for patients, offering a new avenue for tailoring treatments and advancing therapeutic strategies for lung cancer bone metastasis.

Author contributions

Qi Liu: writing – original draft, data curation, formal analysis, investigation, methodology, and visualization. Di Suo: writing – review & editing. Renxian Wang: methodology. Shuai Zhao: visualization. Mao Mao: methodology. Wei-Ning Lee: methodology and resources. Yuhe Yang: supervision and resources. Xin Zhao: supervision, project administration, funding acquisition, resources, and writing – review & editing.

Conflicts of interest

There are no conflicts to declare.

Data availability

All data needed to evaluate the conclusions in the paper are present in the paper and/or the supplementary information (SI).

Supplementary information is available. See DOI: https://doi.org/10.1039/d5lc00951k

Acknowledgements

This work was supported by Collaborative Research with World-leading Research Groups from The Hong Kong Polytechnic University (P0039523). The schematic illustrations in this study were created with BioRender (https://www.biorender.com).

References

1 F. Bray, M. Laversanne, H. Sung, J. Ferlay, R. L. Siegel, I. Soerjomataram and A. Jemal, *Ca-Cancer J. Clin.*, 2024, **74**, 229–263.
2 M. Liu, J. Yang, B. Xu and X. Zhang, *MedComm*, 2021, **2**, 587–617.
3 S. Gerstberger, Q. Jiang and K. Ganesh, *Cell*, 2023, **186**, 1564–1579.
4 B. J. Knapp, S. Devarakonda and R. Govindan, *J. Thorac. Dis.*, 2022, **14**, 1696.
5 Q. Zhang, R. Abdo, C. Iosef, T. Kaneko, M. Cecchini, V. K. Han and S. S.-C. Li, *Nat. Commun.*, 2022, **13**, 5983.
6 D. I. Tsilimigras, P. Brodt, P.-A. Clavien, R. J. Muschel, M. I. D'Angelica, I. Endo, R. W. Parks, M. Doyle, E. de Santibañes and T. M. Pawlik, *Nat. Rev. Dis. Primers*, 2021, **7**, 27.
7 L. Duan, H. L. Pang, W. J. Chen, W. W. Shen, P. P. Cao, S. M. Wang, L. L. Liu and H. L. Zhang, *Oncol. Rep.*, 2019, **41**, 2379–2388.
8 F. Chen, Y. Han and Y. Kang, *Br. J. Cancer*, 2021, **124**, 1912–1920.
9 R. L. Satcher and X. H.-F. Zhang, *Nat. Rev. Cancer*, 2022, **22**, 85–101.
10 Q. Liu, H. Zhang, X. Jiang, C. Qian, Z. Liu and D. Luo, *Mol. Cancer*, 2017, **16**, 176.
11 Y. Li, M. Li, K. Su, S. Zong, H. Zhang and L. Xiong, *Theranostics*, 2023, **13**, 2301.
12 C. Arrigoni, S. Bersini, M. Gilardi and M. Moretti, *Int. J. Mol. Sci.*, 2016, **17**, 1405.
13 Z. Yue, X. Niu, Z. Yuan, Q. Qin, W. Jiang, L. He, J. Gao, Y. Ding, Y. Liu, Z. Xu, Z. Li, Z. Yang, R. Li, X. Xue, Y. Gao, F. Yue, X. H. Zhang, G. Hu, Y. Wang, Y. Li, G. Chen, S. Siwko, A. Gartland, N. Wang, J. Xiao, M. Liu and J. Luo, *J. Clin. Invest.*, 2022, **132**, e144579.
14 W. Hu, Z. Liu, X. Xiao, Y. Yang, Z. Sun and X. Wang, *Cell. Mol. Biol.*, 2020, **66**, 138–142.
15 Y. Wang, Y. Gao, Y. Pan, D. Zhou, Y. Liu, Y. Yin, J. Yang, Y. Wang and Y. Song, *Acta Pharm. Sin. B*, 2023, **13**, 2483–2509.
16 Y. Wang, D. Wu, G. Wu, J. Wu, S. Lu, J. Lo, Y. He, C. Zhao, X. Zhao, H. Zhang and S. Wang, *Theranostics*, 2020, **10**, 300–311.
17 W. Hu, H. P. Bei, H. Jiang, D. Wu, X. Yu, X. Zhou, Q. Sun, Q. Lu, Q. Du, L. Wang, Z. Luo, G. Wu, X. Zhao and S. Wang, *Lab Chip*, 2024, **24**, 3718–3727.
18 S. Lu, F. Cuzzucoli, J. Jiang, L. G. Liang, Y. Wang, M. Kong, X. Zhao, W. Cui, J. Li and S. Wang, *Lab Chip*, 2018, **18**, 3379–3392.
19 C. F. Monteiro, I. A. Deus, I. B. Silva, I. F. Duarte, C. A. Custódio and J. F. Mano, *Adv. Funct. Mater.*, 2024, **34**, 2315940.
20 F. Conceição, D. M. Sousa, J. Loessberg-Zahl, A. R. Vollertsen, E. Neto, K. Søe, J. Paredes, A. Leferink and M. Lamghari, *Mater. Today Bio*, 2022, **13**, 100219.
21 D. E. Glaser, M. B. Curtis, P. A. Sariano, Z. A. Rollins, B. S. Shergill, A. Anand, A. M. Deely, V. S. Shirure, L. Anderson and J. M. Lowen, *Biomaterials*, 2022, **280**, 121245.
22 X. Ji, H. P. Bei, G. Zhong, H. Shao, X. He, X. Qian, Y. Zhang and X. Zhao, *Small*, 2023, **19**, e2207606.
23 M. K. Kim, K. Paek, S. M. Woo and J. A. Kim, *ACS Biomater. Sci. Eng.*, 2023, **9**, 3058–3073.
24 A. Mansoorifar, R. Gordon, R. Bergan and L. E. Bertassoni, *Adv. Funct. Mater.*, 2021, **31**, 2006796.
25 J. Fang, H. Liu, W. Qiao, T. Xu, Y. Yang, H. Xie, C. H. Lam, K. W. K. Yeung and X. Zhao, *Adv. Healthcare Mater.*, 2023, **12**, e2201220.
26 M. Mao, H. P. Bei, C. H. Lam, P. Chen, S. Wang, Y. Chen, J. He and X. Zhao, *Small*, 2020, **16**, e2000546.
27 M. Mao, Z. Meng, J. He and D. Li, *Trends Biotechnol.*, 2024, **42**, 1331–1334.
28 S. Wan, Y. Liu, Y. Weng, W. Wang, W. Ren, C. Fei, Y. Chen, Z. Zhang, T. Wang, J. Wang, Y. Jiang, L. Zhou, T. He and Y. Zhang, *Cell. Oncol.*, 2014, **37**, 363–375.
29 B. Zhang, J. Zhao, H. Yan, Y. Zhao, H. Tian, C. Wang, R. Wang, J. Jin, Y. Chen, C. Yang, C. Li, Y. Jiao, K. Zheng, F. Zhu and W. Tian, *Biomater. Sci.*, 2022, **10**, 1821–1830.
30 M. Mao, J. He, Y. Lu, X. Li, T. Li, W. Zhou and D. Li, *Biofabrication*, 2018, **10**, 025008.
31 A. Adamo, P. Delfino, A. Gatti, A. Bonato, P. Takam Kamga, R. Bazzoni, S. Ugel, A. Mercuri, S. Caligola and M. Krampera, *Front. Cell Dev. Biol.*, 2020, **8**, 584232.
32 Z. H. Li, Y. Si, G. Xu, X. M. Chen, H. Xiong, L. Lai, Y. Q. Zheng and Z. G. Zhang, *Mol. Med. Rep.*, 2017, **16**, 8380–8384.
33 Z. D. Frankman, L. Jiang, J. A. Schroeder and Y. Zohar, *Micromachines*, 2022, **13**, 152.
34 Y. Zheng, J. Chen and J. A. López, *Nat. Commun.*, 2015, **6**, 7858.
35 M. Mao, P. Chen, J. He, G. Zhu, X. Li and D. Li, *Small*, 2022, **18**, e2108102.
36 L. Liu, X. Qu, Z. Wang, C. Ji, R. Ling and C. Yan, *Front. Oncol.*, 2025, **15**, 1602225.
37 S. S. Kotha, B. J. Hayes, K. T. Phong, M. A. Redd, K. Bomsztyk, A. Ramakrishnan, B. Torok-Storb and Y. Zheng, *Stem Cell Res. Ther.*, 2018, **9**, 77.
38 S. P. Cavnar, A. D. Rickelmann, K. F. Meguiar, A. Xiao, J. Dosch, B. M. Leung, S. Cai Lesher-Perez, S. Chitta, K. E. Luker, S. Takayama and G. D. Luker, *Neoplasia*, 2015, **17**, 625–633.
39 J. Huang, P. Woods, D. Normolle, J. P. Goff, P. V. Benos, C. J. Stehle and R. A. Steinman, *Breast Cancer Res. Treat.*, 2017, **161**, 229–243.
40 S. Bakhshandeh, U. Heras, H. M. Taïeb, A. R. Varadarajan, S. M. Lissek, S. M. Hücker, X. Lu, D. S. Garske, S. A. Young and A. Abaurrea, *Sci. Adv.*, 2024, **10**, eadr3997.

41 T. J. Bartosh, M. Ullah, S. Zeitouni, J. Beaver and D. J. Prockop, *Proc. Natl. Acad. Sci. U. S. A.*, 2016, **113**, E6447–E6456.
42 C. M. Ghajar, H. Peinado, H. Mori, I. R. Matei, K. J. Evason, H. Brazier, D. Almeida, A. Koller, K. A. Hajjar, D. Y. Stainier, E. I. Chen, D. Lyden and M. J. Bissell, *Nat. Cell Biol.*, 2013, **15**, 807–817.
43 R. Dai, M. Liu, X. Xiang, Z. Xi and H. Xu, *J. Exp. Clin. Cancer Res.*, 2022, **41**, 316.
44 A. M. Muscarella, S. Aguirre, X. Hao, S. M. Waldvogel and X. H. Zhang, *J. Clin. Invest.*, 2021, **131**, e143764.
45 S. Russo, F. Scotto di Carlo and F. Gianfrancesco, *Front. Cell Dev. Biol.*, 2022, **10**, 886305.
46 L. Endo-Munoz, A. Evdokiou and N. A. Saunders, *Biochim. Biophys. Acta, Rev. Cancer*, 2012, **1826**, 434–442.
47 E. C. G. Díaz, M. Tai, C. E. Monette, J. Y. Wu and F. Yang, *Biomaterials*, 2023, **299**, 122163.